Soft Matter

PAPER

View Article Online
View Journal | View Issue

Cite this: *Soft Matter*, 2015, 11, 7617

Direct observation of drops on slippery lubricant-infused surfaces†

Frank Schellenberger, Jing Xie, Noemí Encinas, Alexandre Hardy, Markus Klapper, Periklis Papadopoulos,‡ Hans-Jürgen Butt* and Doris Vollmer*

Received 22nd July 2015,
Accepted 13th August 2015

DOI: 10.1039/c5sm01809a

www.rsc.org/softmatter

For a liquid droplet to slide down a solid planar surface, the surface usually has to be tilted above a critical angle of approximately 10°. By contrast, droplets of nearly any liquid "slip" on lubricant-infused textured surfaces – so termed slippery surfaces – when tilted by only a few degrees. The mechanism of how the lubricant alters the static and dynamic properties of the drop remains elusive because the drop–lubricant interface is hidden. Here, we image the shape of drops on lubricant-infused surfaces by laser scanning confocal microscopy. The contact angle of the drop–lubricant interface with the substrate exceeds 140°, although macroscopic contour images suggest angles as low as 60°. Confocal microscopy of moving drops reveals fundamentally different processes at the front and rear. Drops recede *via* discrete depinning events from surface protrusions at a defined receding contact angle, whereas the advancing contact angle is 180°. Drops slide easily, as the apparent contact angles with the substrate are high and the drop–lubricant interfacial tension is typically lower than the drop–air interfacial tension. Slippery surfaces resemble superhydrophobic surfaces with two main differences: drops on a slippery surface are surrounded by a wetting ridge of adjustable height and the air underneath the drop in the case of a superhydrophobic surface is replaced by lubricant in the case of a slippery surface.

The macroscopic, apparent wetting properties of surfaces are determined by their surface chemistry and topography on the nano- and micrometre scales.[1,2] Well-designed nano- and microstructured surfaces create the possibility of inducing and controlling new wetting scenarios such as super-liquid repellency.[3,4] Such surfaces include superhydrophobic,[3,5–8] superamphiphobic,[9–12] and slippery lubricant-infused textured surfaces.[13–18] Super-liquid repellency is characterised by particularly low adhesion between the surface and a liquid.[19,20] When a drop of liquid is deposited onto one of these surfaces, it rolls or slides off when the surface is tilted by only a few degrees.[3,5,17] In the case of superhydrophobic or superamphiphobic surfaces, this liquid-repellency is achieved by means of a nano- or microstructured low-energy surface that creates and stabilises air pockets underneath the drop.[3,21–24] As a result, the apparent receding contact angle is greater than 140°, and drops roll off easily.[25]

In the case of slippery lubricant-infused textured surfaces (in short, slippery surfaces), the encapsulated air is replaced by a lubricant that soaks into the textured substrate.[13,14] This lubricant makes the substrate slippery; liquids that would be pinned by the bare textured substrate readily "slip" when the same substrate is infiltrated with a lubricant. The low adhesion of drops to slippery surfaces leads to a broad range of promising applications, ranging from surfaces with anti-biofouling,[26,27] anti-icing,[28,29] and improved heat transfer[15] characteristics to food storage containers.[30] Even ketchup will smoothly flow out of a bottle once the bottle's nanotextured walls have been infiltrated with lubricant.[31] However, the underlying mechanism of how the lubricant changes the shape and motion of drops on slippery surfaces is still under debate due to lack of space and time resolved microscopic information regarding the shape of the buried drop–lubricant interface.

For a drop on a lubricant-infused textured surface, Smith *et al.* have theoretically derived twelve thermodynamically stable wetting configurations as a function of the interfacial tensions, the roughness and the solid fraction.[13] We focus here on those configurations that favor slippery behavior, *i.e.* configurations where the drop does not wet the substrate. The drop may rest on top of the lubricant (Fig. 1A and B), it may sink into the lubricant and rest on top of the protrusions (Fig. 1C and D), or it may penetrate into the textured substrate, thereby replacing the lubricant (not shown). Either the lubricant cloaks the drop (Fig. 1B and D)[13,32,33] or the drop sinks into the lubricant up to a certain height, at which point the lubricant forms an annular wetting ridge around the drop that is pulled above the substrate (Fig. 1A and C).[34–36]

Max Planck Institute for Polymer Research, Ackermannweg 10, 55128 Mainz, Germany. E-mail: vollmerd@mpip-mainz.mpg.de, butt@mpip-mainz.mpg.de

† Electronic supplementary information (ESI) available. See DOI: 10.1039/c5sm01809a

‡ Present address: Department of Physics, University of Ioannina, 45110 Ioannina, Greece.

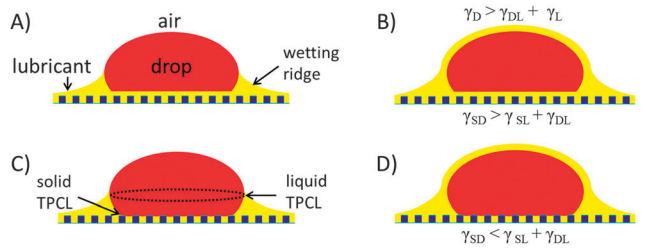

Fig. 1 Wetting configurations. Schematic illustrations of possible wetting configurations of a slippery lubricant-infused textured surface. (A and C) The drop (red) resting on a micropillar array (blue) is surrounded by an annular wetting ridge that may end in a pulled-up liquid three phase contact line (liquid-TPCL). The lubricant (yellow) does not cloak (A and C) or it may cloak (B and D) the drop. Drops on slippery surfaces can exhibit zero, one, or two three-phase contact lines. The liquid-TPLC is the line at which the air, drop, and lubricant meet, and the solid-TPCL is where the substrate, drop, and lubricant meet. The interfacial tensions γ_{ij} are denoted as follows: γ_{DL} – interfacial tension between the drop and the lubricant; γ_{SD} – interfacial tension between the surface and the drop; γ_{SL} – interfacial tension between the surface and the lubricant. γ_D represents the surface tension drop–air and γ_L the surface tension lubricant–air.

The wetting ridge ends in a line, where the air, drop and lubricant meet, which is termed the liquid-three-phase contact line (liquid-TPCL) (Fig. 1C). The line at which the substrate, drop and lubricant meet is hereafter termed the solid-three-phase contact line (solid-TPCL). Depending on the interplay of the interfacial tensions, a slippery surface can exhibit zero (Fig. 1B), one (Fig. 1A and D) or both (Fig. 1C) three-phase contact lines. However, this theoretical prediction does not provide quantitative information on the height and the width of the wetting ridge, the solid-drop contact region, or the dynamics of the liquid- or solid-TPCL. To resolve both, the equilibrium and dynamical behaviour of drops on slippery surfaces, we used laser scanning confocal microscopy.

Experimental

Materials

(Tridecafluoro-1,1,2,2-tetrahydrooctyl)-1-trichlorosilane (97%), FC-70 (97%, C15F33N), 1-butyl-2,3-dimethylimidazolium bis(trifluoromethanesulfonyl)imide $C_{11}H_{17}F_6N_3O_4S_2$ ethylene glycol, hexadecane, and silica nanoparticles (LUDOX SM) were purchased from Sigma-Aldrich, Germany. All chemicals were used without further purification. Microscope glass slides (Menzel, Germany) with a thickness of 170 μm were cleaned with a 2% Hellmanex solution (Hellma, Germany).

Sample preparation

Fabrication of SU-8 pillars. The pillar structures were prepared *via* photolithography using a SU-8 photoresist (Microchem, Germany). Glass slides with a thickness of 170 μm were cleaned with acetone in an ultrasound bath and dried in a vacuum oven (Heraeus) at 170 °C. The SU-8 2025 photoresist was first mixed with the hydrophobic perylenemonoimide dye (PMI) at a concentration of 0.05 mg mL^{-1}.[37] Then, the mixture was spin-coated onto the glass slides. The substrates were then soft baked at 95 °C for 4 min and allowed to slowly cool down for 1 hour. Then they were exposed to UV light (mercury lamp at 350 W) for 35 s (or 30 s) using a Karl-Suss mask aligner and baked at 95 °C for 4 min. The substrates were slowly cooled for 12 h and finally developed with a SU-8 developer (Microchem) and rinsed with 2-propanol. The SU-8 surfaces were treated overnight with 1 M HCl and 0.1 M NaOH at room temperature to hydrolyse the surfaces. Resulting dimensions of the pillars were: center to-center distance 40 μm, diameter 10 μm, and height 10 μm, giving an area fraction of f_{SU8} = 5%. Finally, the surfaces were hydrophobised with (1*H*,1*H*,2*H*,2*H*)-perfluorooctyl-trichlorosilane *via* chemical vapor deposition during 3 h, after activation by O_2 plasma for 0.6 minutes at 150 W. This process increases the density of –OH groups which are anchoring points for the fluorosilane. For this purpose, the substrates and an open glass vessel containing 0.1 mL of the volatile silane were place in a desiccator for 3 hours. The desiccator was evacuated for a few seconds to increase the vapour pressure of the silane. After hydrophobisation, vacuum was applied for one hour to remove unreacted silane residues.

Inverse opals

Monodisperse polystyrene particles (diameter: 1 μm) were synthesised as previously described.[38] An aqueous dispersion of polystyrene particles (1.0 wt%) and silica nanoparticles (0.3 wt%) was prepared. Inverse opals were obtained by lifting a glass substrate out of an aqueous dispersion of polystyrene particles (1.0 wt%) and silica nanoparticle (0.3 wt%) at a lifting speed: 400 nm s^{-1}, at 20 °C and 50% humidity The polystyrene template was removed *via* annealing at 500 °C for 5 hours. The inverse opals surface was activated under O_2 plasma (5 min, 300 W) followed by hydrophobization with (1*H*,1*H*,2*H*,2*H*)-perfluorooctyl-trichlorosilane.

Contact angle measurement

The sliding angles were measured with a contact angle meter (DataPhysics; OCA35). The shapes of the 3 μL drops were fitted using the Young–Laplace equation. All drops were surrounded by a wetting ridge. Therefore, no contact angle could be defined.

Interfacial tension

The surface tension of the used liquids was determined following the pendant drop method (OCA35; DataPhysics, Germany). For comparison, surface tension of the ionic liquid was calculated with a tensiometer using the Wilhelmy plate (DCAT 11EC; DataPhysics, Germany). The pendant drop method was also used to calculate the interfacial tensions of the lubricant–drop systems. For this purpose, approximately 2 mL of the lower density liquid was placed in a cuvette. A drop of the higher-density liquid was suspended on a needle and immersed in the cuvette. The shape profile of the drop was evaluated (Fig. S2, ESI†) and averaged between approximately 50 measurements taken from 5 different droplets. The density values were acquired from the distributor or measured by volume. The variation in the interfacial tension over time was also recorded.

Laser scanning confocal microscopy

The pillar arrays, the lubricants and the advancing and receding contact angles were imaged *via* inverted laser scanning confocal microscopy (LSCM, Leica TCS SP8 SMD) using glass substrates with a thickness of 170 μm. The LSCM had a horizontal resolution of approximately 300 nm and a vertical resolution of approximately 1 μm for the 40× objective. The horizontal resolution of 300 nm can only be achieved for perfectly index matched systems. Depending on the degree of index mismatch and roughness/porosity the horizontal resolution varied between 0.5 μm and 2 μm for the presented data. The spectral ranges could be freely varied, allowing for the simultaneous measurement of the emission signals from different dyes and the reflected light from the interfaces. The ionic liquid and decanol was dyed with Lumogen Red F300 (BASF) FX 67/4 and the water was fluorescently labelled with Alexa Fluor 488 at a concentration of 0.1 mg mL^{-1}. The dyes were excited using the argon line at 488 nm. Care was taken to ensure that the vertical section of the imaging passed through the centre of the drop, as off-centred sections lead to the measurement of incorrect contact angles. Refractive indices; silica: 1.46; FC70: 1.3; water: 1.33; hexadecane: 1.43; SU8: 1.5.

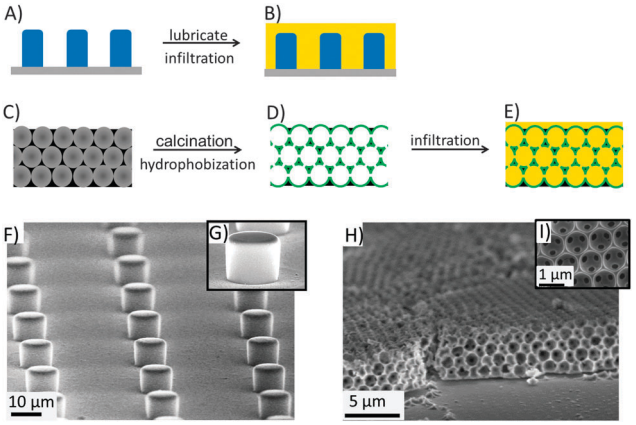

Fig. 2 Schematic illustration of the fabrication of slippery surfaces. (A and B) Cylindrical micropillar arrays (blue) infiltrated with a lubricant (yellow). The dimensions of the pillars employed in this study were as follows: a centre-to-centre distance of 40 μm, a diameter of 10 μm, and a height of 10 μm. (C–E) Inverse opals were obtained by vertical lifting a glass substrate out of an aqueous dispersion of polystyrene particles (diameter: 1 μm) and silica nanoparticles (diameter: 7 nm) and subsequently removing the polystyrene template. The inverse opals (black) were hydrophobised by chemical vapour deposition with perfluorooctyl-trichlorosilane (green) and subsequently infiltrated with a lubricant (yellow). (F–I) Scanning electron microscopy images of (F and G) a micropillar array and of (H and I) an inverse opal.

Scanning electron microscopy

The inverse opals and the pillar arrays were characterised *via* scanning electron microscopy (SEM) using an LEO 1530 Gemini instrument (Zeiss, Oberkochen, Germany) at a low operating voltages (0.7 kV). The cross-sectional images were obtained by tilting the substrate by 75°.

Results and discussion

For the substrates, we investigated micropillar arrays (Fig. 2A, B, F and G) and inverse opals (Fig. 2C–E, H and I) to distinguish between the general and substrate-dependent properties of drops on slippery surfaces. The two systems differ in their morphology and characteristic length scales. The micropillar arrays were fabricated *via* photolithography (methods). The inverse opals were prepared by first depositing a layer of polystyrene and silica particles onto a glass substrate, subsequent calcination of the polystyrene template,[39] followed by hydrophobization of the inverse opals to lower its surface energy. We infiltrated each textured surface with one of the following lubricants: the fluorinated oil FC70, decanol, or the ionic liquid 1-butyl-2,3-dimethylimidazolium bis(trifluoromethanesulfonyl)imide. The choice of these lubricants was motivated by their low surface tension (FC70), low density and low interfacial tension relative to water (decanol), and low volatility (ionic liquid). For the liquid drops, we chose water, peanut-oil, *n*-hexadecane and ethylene glycol because of their greatly differing surface tensions (Table 1). To visualise the lubricants and drops *via* confocal microscopy, we dyed the lubricant, the drop, or both with a fluorescent dye. We imaged lubricants and drops that were not dyed in reflection mode, thereby confirming that the presence of the dye did not influence the results. Care was taken that the chosen dyes were not surface active and were soluble in either the lubricant or the drop.

To gain insight into the macroscopic drop shape, we investigated drops of various surface tensions on inverse opals infiltrated

Table 1 Surface tensions of the drop in presence of lubricant and the lubricant, γ_i, and interfacial tensions between the drop and the lubricant, γ_{ij}. The indices *i* and *j* represent the drop, lubricant, air, or substrate. $S_{D,L} = \gamma_D - \gamma_{DL} - \gamma_L$ is the spreading coefficient of the lubricant (L) on the drop (D) in the presence of vapour. The values did not change over time (Fig. S1 and S2, ESI)

	Water[a] pure, IL, decanol	Decanol	Peanut oil	Ionic liquid (IL)	Hexa-decane	FC70	Ethylene-glycol
γ_i (10^{-3} N m^{-1})	72.1, 44.2 ± 2, 30 ± 5	28.5	35.0	34.6	28.0	17.9	47.3
ρ_i (g cm^{-3})	1.00	0.83	0.92	1.42	0.77	1.93	1.11

	Water–FC70	Water–decanol	Peanut oil–FC70	Water–IL	Hexadecane–FC70	Ethylene-glycol–FC70
γ_{ij} (10^{-3} N m^{-1})	52.8 ± 2	8.6 ± 1	12.0 ± 1	11.4 ± 2	7.1 ± 1	28.2 ± 3
$S_{D,L}$ (10^{-3} N m^{-1})	1.4\pm 2	−7 ± 6	5.1\pm 1	−1.8 ± 4	3.0\pm 1	1.2\pm 2

[a] The surface tension of water can decrease in contact with lubricant. The surface tension of water saturated with the ionic liquid is γ_w(IL) = 44 ± 2 mN m^{-1}, and that of water saturated with decanol is γ_w(dec) = 30 ± 5 mN m^{-1}. Water and FC70 are immiscible, γ_w(FC70) = 72 mN m^{-1}.

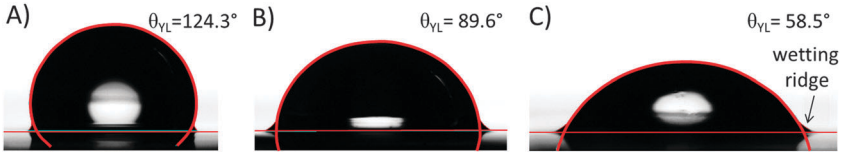

Fig. 3 Drops deposited on a lubricant-infused textured surface. (A) Water, (B) ethylene glycol, and (C) hexadecane drops were placed on inverse opals infiltrated with FC70. The circular red line represents a fit of the drop contour to the Young–Laplace equation. The angles were obtained by fitting the contour of the drop using a Young–Laplace fit. The volume of each drop was 3 μL.

with FC70 using video microscopy (Fig. 3). The drop shape resembled a spherical cap, whose radius of curvature increased as the surface tension of the drop decreased (Table 1). All drops began to slide when the substrate was tilted by less than 2°. The drop contour was fitted using the Young–Laplace equation. The contact angles were determined at the intersections between the horizontal surface and the fit of the cap (red lines, Fig. 3). However, closer inspection of the rims revealed that all drops were surrounded by a wetting ridge. The video microscopy images do not discriminate between the lubricant and the drop. Therefore, the meaning of the angles obtained from the fit is unclear and different from that of the contact angle of a drop on a dry surface. In addition, the concealed lower part of the drop is not visible. Thus, images acquired by video microscopy were insufficient to gain insight how and why the lubricant changes the behaviour of drop on slippery surfaces.

To optically resolve the shape and the dynamics of drops on slippery surfaces with micrometre resolution, we used laser scanning confocal microscopy, subsequently termed confocal microscopy.[40,41] We simultaneously recorded the fluorescence of the lubricant or the drop, and the light reflected from interfaces with sufficient refractive index mismatch. We imaged vertical sections of water drops deposited on micropillar arrays infiltrated with FC70 (Fig. 4A and B), decanol (Fig. 4C and D), and ionic liquid (Fig. 4E and F). Before the water drop was deposited, the thickness of the lubricating film was adjusted to fit the height of the pillars. Therefore, we removed excess lubricant with a tissue and waited until the system had equilibrated. Next, we measured the film thickness at different locations over an area of ≈ 1 cm^2 by confocal microscopy. After confirming that the thickness of the lubricating layer was identical within the studied region, a water drop was gently deposited. First, we investigated the shape of the wetting ridge to decide whether a liquid-TPCL existed. For water on FC70, a thin fluorescent line extending from the upper-left edge of the wetting ridge was visible (Fig. 4A). Water drops on FC70 apply a large capillary force, pulling the wetting ridge up (Fig. 1B). Its height exceeded the field of view, which was 180 μm. We deduce that the FC70 cloaked the drop (Fig. 1B or D). Cloaking requires a positive spreading coefficient $S_{D,L} = \gamma_D - \gamma_{DL} - \gamma_L$. Here, γ_D is the surface tension of the drop saturated with lubricant, γ_L is the surface tension of the lubricant, and γ_{DL} is the interfacial tension between the drop and the lubricant. Indeed, $S_{w,FC70} > 0$ (Table 1). The equilibrium thickness of the cloaking film B can be calculated by equating the capillary pressure in the cloaking film caused by the drop curvature, $2\gamma_{FC70}/R$, and the disjoining pressure, Π_D. van der Waals forces lead to an effective repulsive disjoining pressure between the water–FC70 and the FC70–air interfaces: $\Pi_D = A_H/(6\pi B^3)$. The Hamaker constant A_H quantifies the strength of interaction between the molecules of the phases in contact. Thus, the film thickness is:

$$B = \left(\frac{A_H R}{12\pi\gamma_{FC70}}\right)^{1/3} \quad (1)$$

By estimating the Hamaker constant[42] for the air–water–FC70 interface to be 6×10^{-21} J and for a measured radius of the drop of $R = 1$ mm, we conclude the film thickness to be ≈ 20 nm.

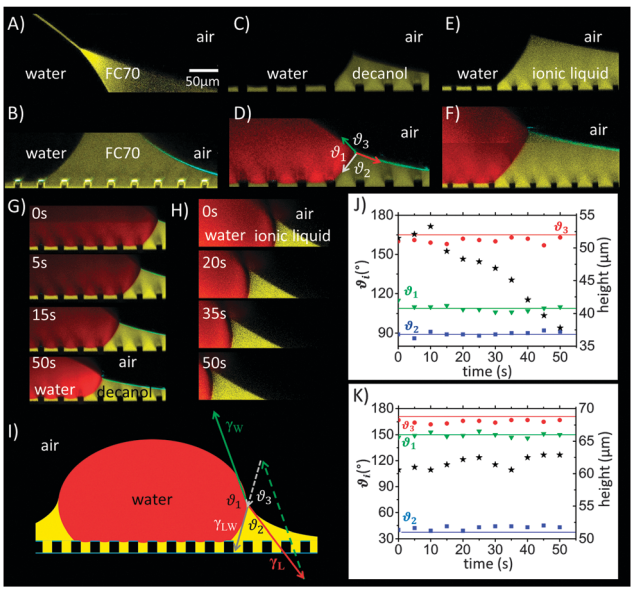

Fig. 4 Cloaking of drops or a liquid-three phase contact line. (A–F) Confocal images of vertical sections through a water drop placed on lubricant-impregnated micropillar arrays (black rectangles). FC70, decanol and ionic liquid were used as lubricants. (A and B) Fluorescence signals (yellow) of FC70 and the reflection of light from the lubricant–air interface (cyan). (C and D) Fluorescence signals (yellow) of decanol. The combined image (D) shows the fluorescence signal of the lubricant, the water drop (red) and reflection of light (cyan). (E and F) Fluorescence signals (yellow) of ionic liquid. The combined image (F) shows the fluorescence signal of the lubricant, the water drop (red) and reflection of light (cyan). (G and H) Time series of an evaporating water drop on (G) a decanol and (H) an ionic liquid lubricated micropillar array. (I) Sketch of the Neumann triangle with the interfacial tensions and the contact angles ϑ_i. Measured and calculated contact angles (left) and the height of the wetting ridge for a water drop deposited on (J) a decanol lubricated micropillar array and (K) an ionic liquid lubricated micropillar surface. The solid lines show the calculated angles according to eqn (2). The ϑ_i are defined according to (I).

By contrast, water drops that were deposited on decanol (Fig. 4C) or ionic liquid (Fig. 4E) were uncloaked, leading to a liquid-TPCL (Fig. 4D–H). Both lubricants acted as surfactants, thereby reducing the surface tension of water (Table 1). The reduced surface tension of the water drop saturated with decanol or ionic liquid[43] led to a negative spreading coefficient and the formation of a liquid-TPCL.

At the liquid-TPCL, the three interfaces (air–drop, air–lubricant, and drop–lubricant interfaces) mutually form three angles ϑ_i. The three angles can be described by the so called Neumann triangle, which relate the interfacial tensions of the three fluid interfaces to the angles formed between those interfaces[33,44,45] (Fig. 4J):

$$\cos\vartheta_1 = \frac{{\gamma_L}^2 - {\gamma_W}^2 - {\gamma_{LW}}^2}{2\gamma_W\gamma_{LW}}, \quad \cos\vartheta_2 = \frac{{\gamma_W}^2 - {\gamma_L}^2 - {\gamma_{LW}}^2}{2\gamma_L\gamma_{LW}}, \quad \cos\vartheta_3 = \frac{{\gamma_{LW}}^2 - {\gamma_W}^2 - {\gamma_L}^2}{2\gamma_W\gamma_L} \tag{2}$$

Eqn (2) are based on the requirement that in mechanical equilibrium, the sum of the horizontal and vertical components of the interfacial tensions acting on the liquid-TPCL must be zero. Within experimental resolution, the Neumann angles do not change while the size of the water drop decreases due to evaporation (Fig. 4G–K, Video 1, ESI†). This can be understood as the angles are determined by the interfacial tensions that do not depend on the drop size. The experimental and calculated angles agree for both lubricants. The height of the wetting ridge $h(t)$ remains constant as long as the height of the drop is large compared to the height of the wetting ridge (Fig. 4K). The variations of $h(t)$ result from the successive depinning events because the wetting ridge needs to adjust to the modified drop shape. Only when the height of the drop approaches the height of the wetting ridge $h(t)$ does decrease (Fig. 4I). This is accompanied with a decreasing curvature of the lubricant–air interface.

Thus far, it remains also unclear whether the drop and substrate are separated by a continuous film of lubricant (Fig. 1A and B) or whether the drops contact the textured substrates directly (Fig. 1C and D). When focusing on the concealed region below the drop, we observed no evidence of fluorescence on top of the pillars (Fig. 4B, C and E). This result suggests that the top faces were not wetted by the lubricant but rather that all drops directly contacted the top of the micropillar arrays (Fig. 1C or D). This observation did not vary with the density difference: decanol has a lower density than water, whereas the ionic liquid and FC70 have a higher density (Table 1). Thus, the gravitational force was negligible compared with capillary forces.

We investigated the shape of the wetting ridge in detail. Fig. 5A shows a vertical section through the wetting ridge surrounding an ethylene glycol drop placed on an inverse opal infiltrated with FC70. The inverse opal structure was overfilled by 10 ± 1 μm before the ethylene glycol drop was deposited. At large distances from the drop (about 4 mm from its centre), the thickness of the lubricating FC70 film was the same as the initial thickness of the lubricating film, 10 ± 1 μm.

The thickness of the wetting ridge gradually increased at distances approaching the drop and the height of the wetting ridge exceeded 250 μm next to the drop. The shape of the lubricant–air interface in equilibrium is governed by the Young–Laplace equation

$$P = 2\gamma C(r) - \rho g z(r) \tag{3}$$

Here, $C(r)$ is the mean curvature at a given point of the interface, $z(r)$ is the height of the wetting ridge, r is the distance from the drop center and P is the pressure in the wetting ridge. Assuming rotational symmetry, the mean curvature of the lubricant–air interface is given by[32,46]

$$2C = \frac{z''}{(1+z'^2)^{3/2}} + \frac{z'}{r}\frac{1}{(1+z'^2)^{1/2}}, \quad \text{where } z' = \frac{\partial z}{\partial r},\ z'' = \frac{\partial^2 z}{\partial r^2} \tag{4}$$

Because at infinite distance the lubricant–air interface is planar, the mean curvature and the Laplace pressure are zero. If we neglect the hydrostatic pressure, the mean curvature is zero everywhere. By setting $\tan f(r) \equiv z'(r)$ and transforming eqn (4) to $(r \sin f)' = 0$ and integrating, we get $z'(r) = \frac{R_0}{\sqrt{r^2 - {R_0}^2}}$. Thus the height $z(r)$ of the wetting ridge should be described by a catenoid $z(r) = R_0 ar\cosh(r/R_0)$, where R_0 is a constant.[33,44]

However, the fit of the lubricant–air interface (Fig. 5B, green line) does not well describe the experimental data (Fig. 5B, black squares), implying that the assumption of zero pressure everywhere was false. To take hydrostatic pressure, $P = -\rho g z(r)$, into account we made an approximation for the case $z'(r) \ll 1$. This assumption is reasonable as the largest value for $z'(r)$ was about 0.25 near the liquid-TPCL and it is much lower far from the liquid-TPCL. In this case the denominators in (eqn (4)) can be neglected, resulting in $\frac{P}{\gamma} = z'' + \frac{z'}{r} \Rightarrow -\frac{z}{{\lambda_c}^2} = z'' + \frac{z'}{r}$, where

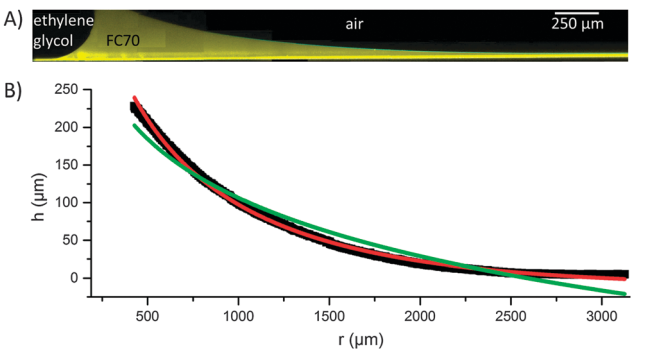

Fig. 5 Shape of the wetting ridge. (A) Extent of the wetting ridge of the FC70 (yellow) which formed after an ethylene glycol drop (black) was deposited on an inverse opal infiltrated with FC70. To span the full, wide range of the wetting ridge (approximately 3 mm, B), various images were combined (each image covered a width of merely 400 μm). (B) Meniscus of FC70 around an ethylene glycol drop on an inverse opal fitted with different models. Red: catenoid; green: nodoid, $C_0 \neq 0$, with fixed pressure P. The experimental data for the height of the wetting ridge $z(r)$ is shown as a function of the distance from the drop center r (black squares). $h = 0$ corresponds to the top face of the pillars.

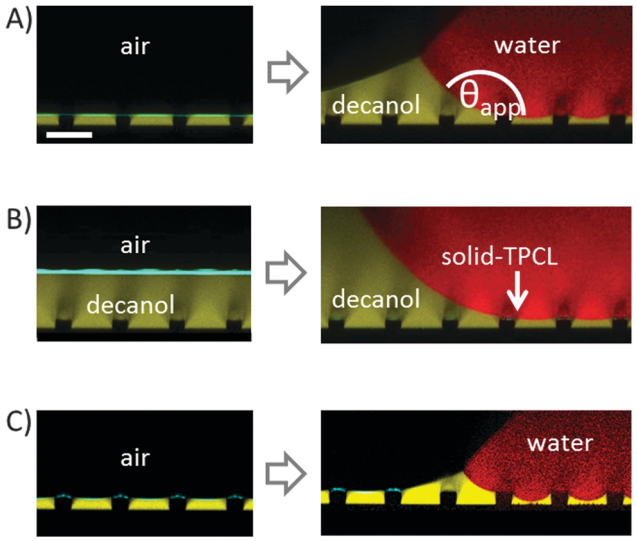

Fig. 6 Influence of the filling height. Image of a micropillar array infiltrated with decanol before (left) and after (right) a water drop was deposited. (A) The height of the lubricant film was adjusted to the height of the micropillar array. (B) The micropillar array was overfilled with lubricant (left) before the water drop was deposited (right). (C) The micropillar array was underfilled before the drop was deposited. The height of overfilling or underfilling was measured relative to the height of the pillar's top face (h = 0 μm). Colour code: Water drop – red; lubricant – yellow; reflected light – cyan; air – black. Diameter of a pillar: 10 μm; height of pillar: 10 μm; centre to centre distance: 40 μm.

λ_c is the capillary length $\lambda_c = \left(\frac{\gamma}{\rho g}\right)^{1/2}$. After the transformation $r = \lambda_c{}^* x$, the equation is the Bessel differential equation. The solution that has only positive values and does not diverge at infinity is the modified Bessel function of the second kind $K_0(x)$, which is approximately equal to $\exp(-x) = \exp(-r/\lambda_c)$.[47] Therefore, we fitted the interface $z(r)$ with this approximate solution (Fig. 5B, red line). For long distances from the centre, $z(r)$ decays exponentially with the capillary length of the lubricant. The good fit supports that hydrostatic pressure is important.

Next we investigated whether the thickness of the lubricating layer influences the shape of the wetting ridge or the shape of the drop (Fig. 6). After we adjusted the height of the lubricant film to the height of the micropillar array (Fig. 6A, left), a water drop was deposited (Fig. 6A, right). The water drop was surrounded by an annular wetting ridge with a height of 50 ± 1 μm, ending at the liquid-TPCL. At the solid-TPCL, the water drop sharply bends upwards, forming an apparent contact angle of $\theta_{app} = 160^\circ \pm 3^\circ$ with the micropillar array. Fig. 6B shows an identical micropillar array that was overfilled by 32 ± 1 μm with lubricant before the water drop was deposited. The height of the wetting ridge increased by more than 100 μm compared to no overfilling, exceeding the field of view (90 μm). The apparent contact angle of the drop with the micropillar array remained constant, $\theta_{app} = 166^\circ \pm 3^\circ$. When the micropillar array was underfilled by 1–2 μm, the height of the wetting ridge decreased to 2–3 μm. The maximum underfilling that can be achieved until the water drop wets the micropillar array depends on the topography and the interaction between the drop–lubricant–substrate. Again, the apparent contact angle is large, $\theta_{app} = 158^\circ \pm 5^\circ$. From these investigations we conclude that the apparent solid contact angle does neither depend on details of how the textured surface is filled nor on the film thickness. However, the degree of overfilling changes the height and range of the wetting ridge. Independent of the initial height of the lubricating layer, the drop squeezed out the lubricant from the concealed lower side of the drop and rests on the pillars top faces. Small drops or underfilling can even induce a negative Laplace pressure, pressing the drop into the textured structure.

Video microscopy suggested that the apparent contact angle depends on the interfacial tension of the drop (Fig. 3). To investigate the dependence of the solid-TPCL on the interfacial tension of the drop, we overfilled the textured surface by approximately 10–25 μm to achieve better visualisation. We monitored the lubricating film far from the drop centre (Fig. 7, left column), at the solid-TPCL (middle column) and below the drops (right column) of various surface tensions that were deposited on inverse opals infiltrated with FC70 (Fig. 7A–C). Far from the drop, the lubricating film was flat. Within experimental accuracy, its thickness matched those before the drop was deposited. All drops exhibited a high but finite "real" apparent contact angle at the solid-TPCL (Fig. 7A–C centre). The apparent contact angles were $\theta_{app} = 174^\circ \pm 3^\circ$ for water, $\theta_{app} = 175^\circ \pm 3^\circ$ for peanut oil and $\theta_{app} = 175^\circ \pm 2^\circ$ for hexadecane. Notably, the apparent contact angle for hexadecane exceeded the values suggested by a Young–Laplace fit of the drop contour (58.5°, Fig. 3C) by more than 100°. For easier comparison of the shape of the drop according to video microscopy and confocal microscopy, Fig. 7D and E show the corresponding images next to each other.

High-magnification images of the contact region below the drop (Fig. 7, right column) revealed that the drops did not penetrate the structure but rested on top of it. The thickness of the lubricating film matched the height of the inverse opal (approximately 4–5 μm, Fig. 2H). This implies that for drops of different interfacial tension, the height of the lubricating layer under the drop is independent from the degree of overfilling.

Confocal microscopy also allows us to analyse how a drop recedes on a lubricant-infiltrated substrate. To induce a slow and controlled recession of the solid-TPCL, we let water drops evaporate and monitored the receding contact line. As an example, one sequence of a water drop evaporating from an FC70-infiltrated microarray is shown in Fig. 8A and B (Video 2, ESI†). At time t = 0, the drop was pinned at its outer-right edge (Fig. 8A). The apparent contact angle was $\approx 160^\circ$. During evaporation, the apparent receding contact angle decreased until it reached its apparent receding contact angle, $\theta_{r,app} = 144^\circ \pm 2^\circ$. Within less than 3 s, the contact line moved to the left-hand side of the pillar and depinned. Depinning was accompanied by an abrupt increase in the apparent contact angle. Immediately following depinning, the apparent contact angle increased to values as large as 170° (Fig. 8B) and the process repeated. The contact angle decreased until it reached its receding value of $\theta_{r,app} = 144^\circ \pm 1^\circ$ (t = 320 s), thus initiating another depinning event. The time span between successive depinning events

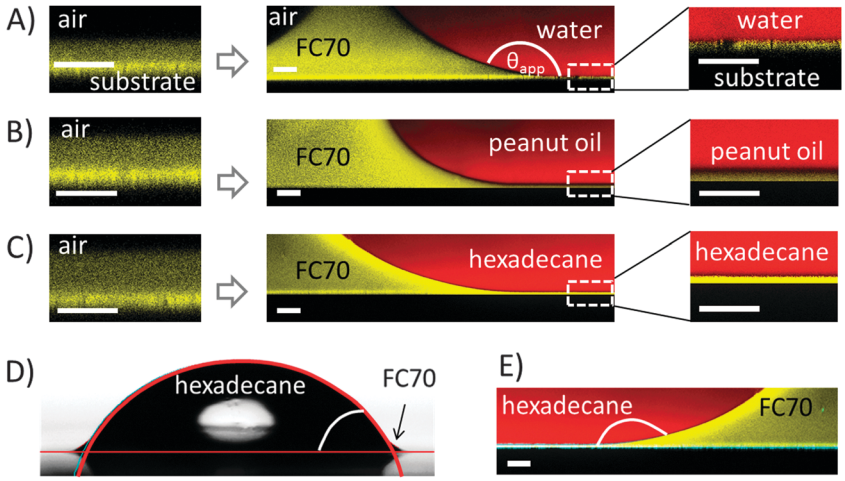

Fig. 7 Vertical cross sections through liquid drops on slippery inverse opals. (A–C) Show the shapes of the lubricant–air and drop–lubricant–substrate interfaces of different drops: (A) water, (B) peanut oil, (C) hexadecane. Left: Approximately 4 mm from the drop; middle: drop–lubricant–substrate contact line; right: under the drop. θ_{app} denotes the apparent contact angle. The reflection (cyan) signal indicates the lubricant–air, lubricant-infiltrated-inverse-opal and opal–glass interfaces. Care was taken to ensure that the vertical section of the imaging always passed through the centre of the drop. (D and E) Comparison of an image of a hexadecane drop on a FC70 infused inverse opal taken by (D) video microscopy and (E) confocal microscopy. Colour code: Drop – red; lubricant – yellow; reflected light – cyan; air – black scale bars in (A) to (C): left and right: 10 μm, centre column: 30 μm, (E): 30 μm. (D) Drop volume: 3 μL. The height of overfilling was measured with respect to the top surface of the inverse opals.

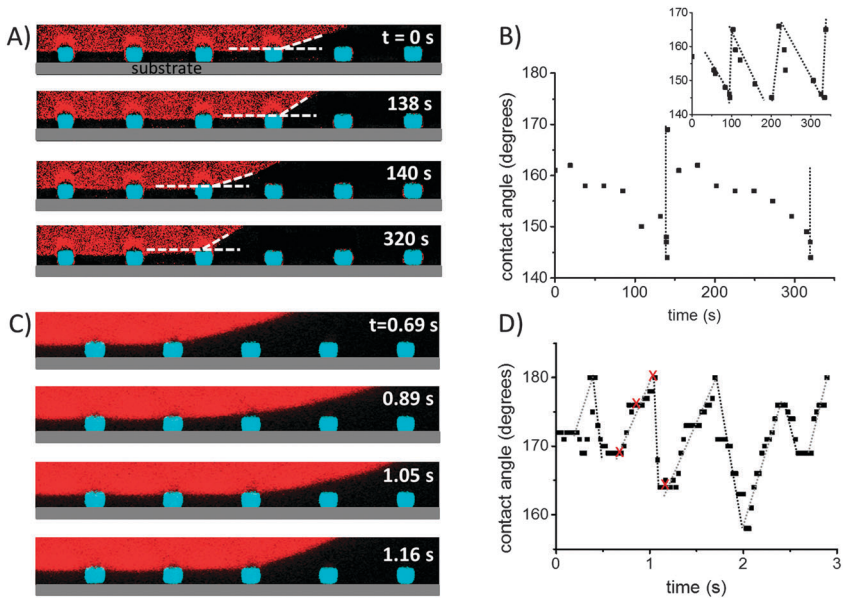

Fig. 8 Receding and advancing contact angles at the solid-TPCL. (A) Confocal microscopy images monitoring the contact angle of a water drop (red) as it recedes because of evaporation on an FC70-impregnated micropillar array (blue). The FC70 was not dyed. (B) The contact angle continuously decreased until it approached the receding contact angle, $\theta_{r,app} = 144^\circ \pm 1^\circ$. Inset: Variation in θ_{app} for a water drop on a micropillar array impregnated with the ionic liquid. (C) Confocal microscopy images monitoring the advancement of a drop on an FC70-impregnated micropillar array. Advancement was induced by applying air flow. (D) Variation in θ_{app} as the drop advanced. The contact angle continuously increased until it reached 180° and subsequently abruptly decreased to a lower value. The crosses correspond to the images shown in C. The receding ($v_{rec} = 0.18 \pm 0.05$ μm s^{-1}) and advancing ($v_{adv} = 60.5 \pm 6.5$ μm s^{-1}) velocities were averaged over the time required to recede/advance over three pillars.

varied slightly, which can be understood by considering that depinning is a three-dimensional process, so the next nearest neighbours that were wetted by the drop influenced the curvature of the drop. The receding contact angle depends on the width of and the spacing between pillars. $\theta_{r,app}$ also depends on the interfacial tensions between the pillars' top face and the lubricant or liquid.

The depinning of the water from the ionic liquid proceeded almost identically. Even the receding contact angle barely differed: $\theta_{r,app}(IL) = 144^\circ \pm 2^\circ$ (inset of Fig. 8B). Thus, cloaking (which was present on the water drops on FC70 and absent on the water drops on the ionic liquid) did not influence the receding dynamics. On the lubricant-impregnated inverse

opals, the receding contact angle remained above 170°. Because of the smaller spacing within the inverse opal, individual successive depinning events could not be resolved.

To cause the drop to advance, we pushed it forward by applying a weak air flow (Fig. 8C and D). After the drop was deposited, the rightmost contact line was pinned at the right-hand side of the pillar (Fig. 8C, t = 0.69 s). As the drop advanced, the contact line bent downward (Video 3, ESI†). This was accompanied by a continuous increase in the contact angle, which gradually approached $\theta_{r,app}$ = 180°. As soon as the drop–lubricant interface touched the top face of the rightmost pillar, the contact line jumped forward and the contact angle decreased by up to 20° (Fig. 8D). The broad scatter of the contact angles measured during the advancement can be attributed to a higher velocity from slight variations in the air pressure. Within experimental accuracy, we also observed an advancing contact angle of 180° on the inverse opals. Notably, water drops on liquid-impregnated micropillar arrays can exhibit apparent contact angle hysteresis at the solid-TPCL as large as $\Delta\Theta = \theta_{a,app} - \theta_{r,app} \approx 35°$, even when the sliding angle is below 5°. The sliding angles of drops on slippery surfaces α are typically lower than the sliding angles of water drops on superhydrophobic surfaces. Still, α results from a balance between gravity and capillary forces:[48,49]

$$\sin\alpha = \frac{k\gamma_{DL}b}{mg}(\cos\Theta_{r,app} - \cos\Theta_{a,app}) \quad (5)$$

Here, m is the mass of the drop plus the effective mass of the wetting ridge, g = 9.81 m s^{-2}, b is the effective width of the drop in contact with the solid, and $k \approx 1.5$ is a prefactor in the order of 1, which varies depending on the specific shape of the contact area. The reason for the low sliding angle is threefold: (i) as for superhydrophobic surfaces, drops on liquid infused surface move easily because the apparent receding contact angles are high. Indeed, close to the solid-TPCL, the shape of a drop deposited on a superhydrophobic almost matches those on a slippery surface (Fig. 9). The high value of $\Theta_{r,app}$ reduces $\Delta\Theta$ and even for $\Theta_{a,app}$ = 180°, the difference of the cosines is less than 0.2. In addition, the high apparent receding contact angle also leads to a small width of the apparent contact area. In this respect, superhydrophobic and slippery surfaces behave identical. Secondly, drops can move easier on a slippery surface because (ii) the drop–lubricant interfacial tension is typically lower than the drop–air interfacial tension. For example the interfacial tension between water–decanol ($\gamma_{water-decanol}$ = 0.0086 N m^{-1}) is almost one order of magnitude below the water–air interfacial tension ($\gamma_{water-air}$ = 0.072 N m^{-1}). The third reason for low sliding angle is because (iii) the weight of the drop is effectively increased due to the additional mass of the wetting ridge. This effect depends on the height of the wetting ridge compared to the size of the drop. It is typically small for mm sized drops but can become significant for small drop sizes. Taking these effects into account, the tilting angle for a water drop with a radius of R = 1 mm deposited on an ionic liquid infused slippery surface can be estimated to be α = 3° (eqn (5)), where k = 1.5, $\gamma_{water-IL}$ = 0.011 N m^{-1}, b = 0.8 ± 0.2 mm, m = 4 × 10^{-6} kg, $\Theta_{r,app}$ = 145° and $\Theta_{a,app}$ = 180°. Within experimental accuracy, the sliding angle matches the measured angle, α = 3 ± 1°. Remarkably, despite the presence of the wetting ridge, the receding dynamics of a drop on a slippery surface (Fig. 8) resemble those on a superhydrophobic surface.[20,37]

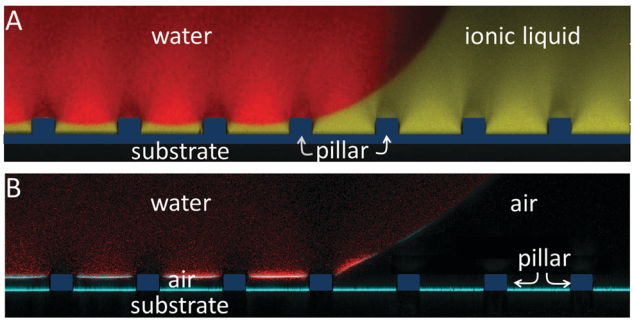

Fig. 9 Slippery compared to superhydrophobic surface. Comparison of a water droplet (red) deposited on (A) a slippery ionic liquid (yellow) infused micropillar array (dark blue stimulated pillars), (B) a superhydrophobic surface. Air, glass substrate and the micropillar arrays appear black. On a slippery micropillar array the drop rests on the pillars' top faces and the region between the micropillars is filled with lubricant. On the super-hydrophobic surface the interpillar space is filled with air. Image size: 291.6 × 71.7 μm^2.

In summary, we have shown that receding and advancing of the rim of a drop are fundamentally different processes. Drops recede through well-defined depinning events. For the advancing contact line, no critical contact angle exists. The drop–lubricant interface gradually bends downwards until it touches the top face of the foremost protrusion. The high apparent contact angles, the small width of the contact area, the low interfacial tension and the increased effective mass of the drop result in easy sliding of the drop. Consistent with theory, drops can be cloaked by a thin lubricant film or surrounded by an annular wetting ridge. The range and the height of the wetting ridge can be tuned by the thickness of the lubricant layer. Gravity can influence the shape of the meniscus, resulting in a finite pressure in the wetting ridge. The angles at the solid- and liquid-TPCL are determined by the choice of materials but do not depend on the shape, range and height of the wetting ridge.

Author contributions

D.V. and H.J.B. conceived and supervised the research. F.S. performed the confocal imaging and the analysis. J.X. fabricated the inverse opals and N.E. fabricated the micropillar arrays. A.H., J.X., and N.E. measured the contact angles *via* optical microscopy and N.E. measured the interfacial tensions and P.P. estimated the Laplace pressure. M.K. offered the fluorinated dye. All authors contributed in writing and revising the manuscript.

Acknowledgements

We thank G. Glasser, G. Schäfer, T. Schuster and M. Wagner for technical support, and K. Varanasi, T. Kajiya and G. Auernhammer for stimulating discussions, and J. Pham for carefully reading

the manuscript. Financial support from SPP 1420 (H.J.B.), COST1106 (D.V.), and ERC grant SuPro (H.J.B.) is gratefully acknowledged.

References

1 P. G. de Gennes, Wetting – statics and dynamics, *Rev. Mod. Phys.*, 1985, **57**, 827–863.
2 D. Bonn, J. Eggers, J. Indekeu, J. Meunier and E. Rolley, Wetting and spreading, *Rev. Mod. Phys.*, 2009, **81**, 739–805, DOI: 10.1103/RevModPhys.81.739.
3 D. Quere, Non-sticking drops, *Rep. Prog. Phys.*, 2005, **68**, 2495–2532, DOI: 10.1088/0034-4885/68/11/r01.
4 H. Kusumaatmaja and J. M. Yeomans, Modeling contact angle hysteresis on chemically patterned and superhydrophobic surfaces, *Langmuir*, 2007, **23**, 6019–6032, DOI: 10.1021/la063218t.
5 W. Barthlott and C. Neinhuis, Purity of the sacred lotus, or escape from contamination in biological surfaces, *Planta*, 1997, **202**, 1–8.
6 L. Feng, *et al.*, Super-hydrophobic surfaces: From natural to artificial, *Adv. Mater.*, 2002, **14**, 1857–1860, DOI: 10.1002/adma.200290020.
7 P. Roach, N. J. Shirtcliffe and M. I. Newton, Progress in superhydrophobic surface development, *Soft Matter*, 2008, **4**, 224–240, DOI: 10.1039/b712575p.
8 A. Nakajima, *et al.*, Transparent superhydrophobic thin films with self-cleaning properties, *Langmuir*, 2000, **16**, 7044–7047, DOI: 10.1021/la000155k.
9 A. Tuteja, *et al.*, Designing superoleophobic surfaces, *Science*, 2007, **318**, 1618–1622, DOI: 10.1126/science.1148326.
10 X. Deng, L. Mammen, H.-J. Butt and D. Vollmer, Candle soot as a template for a transparent robust superamphiphobic coating, *Science*, 2012, **335**, 67–70.
11 M. Paven, *et al.*, Super liquid-repellent gas membranes for carbon dioxide capture and heart–lung machines, *Nat. Commun.*, 2013, **4**, 2512, DOI: 10.1038/ncomms3512.
12 B. Leng, Z. Shao, G. de With and W. Ming, Superoleophobic Cotton Textiles, *Langmuir*, 2009, **25**, 2456–2460, DOI: 10.1021/la8031144.
13 J. D. Smith, *et al.*, Droplet mobility on lubricant-impregnated surfaces, *Soft Matter*, 2013, **9**, 1772–1780, DOI: 10.1039/c2sm27032c.
14 A. Lafuma and D. Quere, Slippery pre-suffused surfaces, *EPL*, 2011, **96**, 56001.
15 K. Rykaczewski, *et al.*, Dropwise condensation of low surface tension fluids on omniphobic surfaces, *Sci. Rep.*, 2014, **4**, 4158, DOI: 10.1038/srep04158.
16 A. K. Epstein, T.-S. Wong, R. A. Belisle, E. M. Boggs and J. Aizenberg, Liquid-infused structured surfaces with exceptional anti-biofouling performance, *Proc. Natl. Acad. Sci. U. S. A.*, 2012, **109**, 13182–13187, DOI: 10.1073/pnas.1201973109.
17 T.-S. Wong, *et al.*, Bioinspired self-repairing slippery surfaces with pressure-stable omniphobicity, *Nature*, 2011, **477**, 443–447.
18 J. Zhang, A. Wang and S. Seeger, Nepenthes Pitcher Inspired Anti-Wetting Silicone Nanofilaments Coatings: Preparation, Unique Anti-Wetting and Self-Cleaning Behaviors, *Adv. Funct. Mater.*, 2014, **24**, 1074–1080, DOI: 10.1002/adfm.201301481.
19 D. W. Pilat, *et al.*, Dynamic measurement of the force required to move a liquid drop on a solid surface, *Langmuir*, 2012, **28**, 16812–16820.
20 B. M. Mognetti and J. M. Yeomans, Modeling receding contact lines on superhydrophobic surfaces, *Langmuir*, 2010, **26**, 18162–18168, DOI: 10.1021/la103539m.
21 H.-J. Butt, *et al.*, Design principles for superamphiphobic surfaces, *Soft Matter*, 2013, **9**, 418–428.
22 B. Bhushan and Y. C. Jung, Natural and biomimetic artificial surfaces for superhydrophobicity, self-cleaning, low adhesion, and drag reduction, *Prog. Mater. Sci.*, 2011, **56**, 1–108, DOI: 10.1016/j.pmatsci.2010.04.003.
23 N. A. Patankar, On the modeling of hydrophobic contact angles on rough surfaces, *Langmuir*, 2003, **19**, 1249–1253, DOI: 10.1021/la026612+.
24 C. W. Extrand, Model for contact angles and hysteresis on rough and ultraphobic surfaces, *Langmuir*, 2002, **18**, 7991–7999, DOI: 10.1021/la025769z.
25 Q. D. Xie, *et al.*, Facile creation of a super-amphiphobic coating surface with bionic microstructure, *Adv. Mater.*, 2004, **16**, 302–305, DOI: 10.1002/adma.200306281.
26 D. C. Leslie, *et al.*, A bioinspired omniphobic surface coating on medical devices prevents thrombosis and biofouling, *Nat. Biotechnol.*, 2014, **32**, 1134–1140.
27 N. Vogel, R. A. Belisle, B. Hatton, T.-S. Wong and J. Aizenberg, Transparency and damage tolerance of patternable omniphobic lubricated surfaces based on inverse colloidal monolayers, *Nat. Commun.*, 2013, **4**, 2176, DOI: 10.1038/ncomms3176.
28 P. Kim, *et al.*, Liquid-Infused Nanostructured Surfaces with Extreme Anti-Ice and Anti-Frost Performance, *ACS Nano*, 2012, **6**, 6569–6577, DOI: 10.1021/nn302310q.
29 S. B. Subramanyam, K. Rykaczewski and K. K. Varanasi, Ice Adhesion on Lubricant-Impregnated Textured Surfaces, *Langmuir*, 2013, **29**, 13414–13418, DOI: 10.1021/la402456c.
30 S. B. Subramanyam, K. Rykaczewski and K. K. Varanasi, *Self-lubricating surfaces for food packing and food processing equipment*, *US Pat.*, 201302519522013.
31 https://www.youtube.com/watch?v=NF4LQW1RDCc.
32 H. M. Princen and S. G. Mason, Shape of a fluid drop at a fluid-liquid interface. II. Theory for three-phase systems, *J. Colloid Sci.*, 1965, **20**, 246–266.
33 H. M. Princen, in *Surface and Colloid Science*, ed. E. Matijevic, Wiley-Interscience, 1969, vol. 2, p. 254.
34 A. Carre, J. C. Gastel and M. E. R. Shanahan, Viscoelastic effects in the spreading of liquids, *Nature*, 1996, **379**, 432–434, DOI: 10.1038/379432a0.
35 C. W. Extrand and Y. Kumagai, Contact angles and hysteresis on soft surfaces, *J. Colloid Interface Sci.*, 1996, **184**, 191–200.
36 R. Sokuler, *et al.*, The softer the better: Fast condensation on soft surfaces, *Langmuir*, 2010, **26**, 1544–1547.

37 P. Papadopoulos, L. Mammen, X. Deng, D. Vollmer and H.-J. Butt, How superhydrophobicity breaks down, *Proc. Natl. Acad. Sci. U. S. A.*, 2013, **110**, 3254–3258.
38 M. D'Acunzi, *et al.*, Superhydrophobic surfaces by hybrid raspberry-like particles, *Faraday Discuss.*, 2010, **146**, 35–48.
39 J. Wang, Q. Li, W. Knoll and U. Jonas, *J. Am. Chem. Soc.*, 2006, **128**, 15606–15607.
40 P. Papadopoulos, *et al.*, Wetting on the microscale: shape of a liquid drop on a microstructured surface at different length scales, *Langmuir*, 2012, **28**, 8392–8398.
41 R. Pericet-Camara, A. Best, H.-J. Butt and E. Bonaccurso, Effect of capillary pressure and surface tension on the deformation of elastic surfaces by sessile liquid microdrops: an experimental investigation, *Langmuir*, 2008, **24**, 10565–10568.
42 H.-J. Butt and M. Kappl, *Surface and interfacial forces*, Wiley-VCH, 2010.
43 D. J. Donahue and F. E. Bartell, The boundary tension at water organic liquid interfaces, *J. Phys. Chem.*, 1952, **56**, 480–489.
44 P. G. de Gennes, F. Brochard-Wyart and D. Quéré, *Capillarity and wetting phenomena*, Springer, 2004.
45 A. Marchand, S. Das, J. H. Snoeijer and B. Andreotti, Contact angles on a soft solid: From Young's law to Neumann's law, *Phys. Rev. Lett.*, 2012, **109**, 236101.
46 M. Lipschutz, *Differential Geometry*, Mc Graw-Hill, 1969.
47 G. Arfken, *Modified Bessel Functions, Iv(x) and Kv(x) 610–616*, Academic Press, FL, 1985.
48 A. ElSherbini and A. Jacobi, Retention forces and contact angles for critical liquid drops on non-horizontal surfaces, *J. Colloid Interface Sci.*, 2006, **299**, 841–849.
49 C. G. L. Furmidge, Studies at phase interfaces. I. The sliding of liquid drops on solid surfaces and a theory for spray retention, *J. Colloid Sci.*, 1962, **17**, 309–324.

